Relaxing the Boussinesq Approximation in Ocean Circulation Models

Richard J. Greatbatch[1], Youyu Lu[1] and Yi Cai[2]

[1]Department of Oceanography,
Dalhousie University,
Halifax, Nova Scotia, Canada B3H 4J1

[2]National Research Center for Marine Environmental Forecasts,
8, Dahuisi,
Haidian District, 100081 Beijing, China

Received August 2000; revised March 2001; accepted April 2001 .

Journal of Atmospheric and Oceanic Technology

Short title: NON-BOUSSINESQ OCEAN MODELS

Abstract.

There is a growing need for ocean circulation models that conserve mass rather than volume (as in traditional Boussinesq models). One reason is bottom pressure data expected to flow from satellite-mounted gravity-measuring instruments, and another is to provide a complete interpretation of data from satellite altimeters such as TOPEX-POSEIDON. In this paper, it is shown that existing, hydrostatic Boussinesq ocean model codes can easily be modified, with only a modest increase in the cpu requirement, to integrate the hydrostatic, non-Boussinesq equations. The method can be used to integrate both coarse resolution and eddy-resolving non-Boussinesq models. The basic equations can also be used to formulate a fully non-hydrostatic, non-Boussinesq model. The method is illustrated for the case of POP, the parallel version of the Bryan/Cox/Semtner code developed at Los Alamos National Laboratory. A comparison of eddy-permitting model solutions under double gyre wind forcing shows that the error in making the Boussinesq approximation is, reassuringly, only a few percent. We also consider a coarse resolution global ocean model under seasonal forcing. The non-Boussinesq model shows a seasonal variation in global mean sea surface height (SSH) with a range of about 3 cm, attributable mostly to changes in the mass of the ocean due to the freshwater flux forcing, but with a roughly 25% contribution from the steric expansion effect. The seasonal cycles of model-computed SSH are also compared with TOPEX-POSEIDON data from the South Pacific and South Atlantic Oceans. It is shown that the seasonal cycle in global mean SSH contributes to the model-computed seasonal cycle, and improves the model performance compared to the data. It is found that the difference between the seasonal cycles in the Boussinesq and non-Boussinesq models is almost entirely accounted for by the seasonal cycle in global mean SSH. On the other hand, on longer time scales the difference field between the non-Boussinesq and Boussinesq models shows spatial variability of several centimeters that is not accounted for by a globally uniform correction to the Boussinesq model.

1. Introduction

The new generation of satellite-mounted gravity measuring instruments are expected to measure variability in bottom pressure to an accuracy of 1 mm of equivalent water thickness on scales of several hundred kilometers. An example is GRACE (Gravity Recovery and Climate Experiment) to be launched in mid-2001 (Hughes et al., 2000). The level of accuracy expected from GRACE calls for a re-examination of many conventional approximations often taken for granted by physical oceanographers. Among these is the Boussinesq approximation. Indeed, it is expected that non-Boussinesq models will be required to provide a complete synthesis and interpretation of the data expected to flow from GRACE. Such models also have the advantage that because they conserve mass, rather than volume, they can be used to unambiguously interpret sea level height from tide gauges or satellite altimeters such as TOPEX-POSEIDON. In this paper we describe a procedure for modifying existing, hydrostatic ocean models to relax the Boussinesq approximation and make them non-Boussinesq. The basic equations can also be used to formulate a fully non-hydrostatic, non-Boussinesq code. The code changes we propose are modest and preserve the basic structure of currently existing Boussinesq code. We illustrate the method using POP (Parallel Ocean Program), the parallel version of the Bryan/Cox/Semtner model developed at Los Alamos National Laboratory. For the case of POP, the increase in cpu associated with the changes is no more than $\approx 20\%$.

While it is missions such as GRACE that have brought to the fore the need for mass-conserving ocean models, concern over the accuracy of the Boussinesq approximation has been raised by several authors. Greatbatch(1994) suggested that for applications in which the interest is sea-level rise associated with climate change (e.g. global warming), globally-averaged sea-level from a Boussinesq ocean model can be adjusted by a spatially uniform value chosen to ensure that the mass budget is satisfied in a globally-averaged sense. Greatbatch argued that applying a spatially uniform

correction should be a good approximation to the behaviour of a fully mass-conserving model on time scales long compared to the time scale required to set up the inverse barometer response to atmospheric pressure forcing. Questions have also been raised regarding the accuracy of the tracer equations in Boussinesq ocean models, an issue that is discussed in detail in the companion manuscript by McDougall, Greatbatch and Lu(2001; hereafter MGL), where a detailed discussion of the Boussinesq approximation can be found. MGL argue that concern regarding the tracer equations is removed by interpreting the velocity variable carried by models as the average mass flux per unit area normalised by a constant reference density. MGL also note that using this new velocity variable, the governing equations for a non-Boussinesq ocean take a form very close to that of their Boussinesq counterpart, and that this new set of equations could be used to eliminate the Boussinesq approximation altogether from currently existing Boussinesq ocean model codes. The objective of the present paper is to show how the method suggested by MGL can be implemented numerically, and then to evaluate the model performance, comparing our new non-Boussinesq code with that of the Boussinesq original.

An alternative method for including non-Boussinesq effects in Boussinesq ocean models has been suggested by Lu(2001). Rather than follow Lu, we note that the approach suggested by MGL has the advantage that the conservation properties of the finite difference equations, built into an existing Boussinesq model, can be readily preserved in the new non-Boussinesq code. The method of Lu nonetheless provides a convenient way to analyze our non-Boussinesq model results, as we show in Section 4. There are also several other studies in the published literature that look at non-Boussinesq effects in ocean models. Our approach is closest to that of Mellor and Ezer(1995), although we differ from these authors in the interpretation of the model variables and in the treatment of the equation of state (our approach corrects an error pointed out by Dewar et al., 1998). Another study is that of Dukowicz(1997). However,

Dukowicz does not discuss how his model variables should be interpreted, nor does he consider the error associated with the Boussinesq approximation in the tracer equation. Finally, there is the recent work of Huang et al.(2001a,b). These authors describe a new hydrostatic, non-Boussinesq ocean model, and also some of the difficulties that arise when trying to interpret bottom pressure or sea surface height data using a Boussinesq model. It should be noted, however, that their model is a completely new code, whereas our approach is to make relatively minor changes to currently existing Boussinesq code.

The plan of the remainder of the paper is as follows. In Section 2, we use density-weighted averaging in a fixed coordinate system to set up the governing equations for our model, including the treatment of the kinematic boundary condition at the sea surface. In Section 3, we show how to modify the POP model code to make it fully non-Boussinesq. It should be noted that the approach we propose is actually quite general, and can also be applied to other hydrostatic, Boussinesq model codes. The performance of the new, non-Boussinesq code is compared with its Boussinesq counterpart in Section 4. We consider two different problems: an eddy permitting calculation in a closed, rectangular basin under double-gyre wind forcing, and a coarse resolution global ocean model under seasonal forcing. The latter case is used to show the ability of the non-Boussinesq code to compute the seasonal cycle in global mean sea level. We illustrate the importance of taking proper account of the mass budget of the global ocean by comparing the seasonal cycles of model-computed sea level and TOPEX-POSEIDON altimeter data from the South Atlantic and South Pacific Oceans. Section 5 provides a summary and conclusions, and in the Appendix we summarise the equations governing our non-Boussinesq and Boussinesq models.

2. The governing equations

We begin by writing down the instantaneous equations governing conservation of mass, a conservative scalar, C, and momentum. Following Batchelor(1967) and

Gill(1982), these are

$$\rho_t + \nabla \cdot (\rho \mathbf{u}) = 0, \tag{1}$$

$$(\rho C)_t + \nabla \cdot (\rho \mathbf{u} C) = \nabla \cdot (\rho k_C \nabla C), \tag{2}$$

$$(\rho \mathbf{u})_t + \nabla \cdot (\rho \mathbf{u}\mathbf{u}) + 2\boldsymbol{\Omega} \times (\rho \mathbf{u}) = -\nabla p - \mathbf{k} g \rho + \nabla \cdot (\mu \nabla \mathbf{u}) + \frac{1}{3} \nabla (\mu \nabla \cdot \mathbf{u}). \tag{3}$$

The terminology here is standard, with μ being the viscosity and k_C being the diffusivity of tracer, C. It should be noted that C is defined as the mass of tracer contained in unit mass of fluid (Gill, 1982). C can also be interpreted as potential temperature and, indeed, throughout the following, C is either salinity or potential temperature.

In order to derive the equations governing our non-Boussinesq ocean model, we introduce density-weighted averaging, or Favre-averaging (in a fixed coordinate system) after Favre(1965a,b). We therefore define

$$\overline{\mathbf{u}}^{\rho} = \overline{\rho \mathbf{u}}/\overline{\rho}, \quad \overline{C}^{\rho} = \overline{\rho C}/\overline{\rho}, \quad \mathbf{u}'_{\rho} = \mathbf{u} - \overline{\mathbf{u}}^{\rho} \quad \text{and} \quad C'_{\rho} = C - \overline{C}^{\rho}. \tag{4}$$

where $\overline{\mathbf{u}}^{\rho}$, $\overline{C}^{\rho}$ are the density-weighted averages of velocity $\mathbf{u}$ and tracer concentration, C, respectively, and $\overline{\rho \mathbf{u}'_{\rho}} = \mathbf{0}$ and $\overline{\rho C'_{\rho}} = 0$. Averaging the instantaneous conservation equations, (1) - (3), then leads to

$$\overline{\rho}_t + \nabla \cdot (\overline{\rho}\ \overline{\mathbf{u}}^{\rho}) = 0, \tag{5}$$

$$(\overline{\rho}\,\overline{C}^{\rho})_t + \nabla \cdot (\overline{\rho}\ \overline{\mathbf{u}}^{\rho}\overline{C}^{\rho}) = -\nabla \cdot (\overline{\rho \mathbf{u}'_{\rho} C'_{\rho}}) + \nabla \cdot (\overline{\rho k_C \nabla C}), \tag{6}$$

$$(\overline{\rho}\ \overline{\mathbf{u}}^{\rho})_t + \nabla \cdot (\overline{\rho}\ \overline{\mathbf{u}}^{\rho}\overline{\mathbf{u}}^{\rho}) + 2\boldsymbol{\Omega} \times (\overline{\rho}\ \overline{\mathbf{u}}^{\rho}) = -\nabla \overline{p} - \mathbf{k} g \overline{\rho} - \nabla \cdot (\overline{\rho \mathbf{u}'_{\rho} \mathbf{u}'_{\rho}}) + \nabla \cdot (\overline{\mu \nabla \mathbf{u}}) + \frac{1}{3} \nabla (\overline{\mu \nabla \cdot \mathbf{u}}). \tag{7}$$

Perhaps the major advantage of using density-weighted averaging is that no turbulent correlation terms appear in the averaged mass conservation equation (5), as would appear with conventional Reynolds averaging. Indeed, the form of (5)-(7) closely follows that of the instantaneous equations, (1)-(3).

Following MGL, we introduce a new velocity variable

$$\tilde{\mathbf{u}} \equiv (\rho \mathbf{u})/\rho_o, \tag{8}$$

which when averaged, becomes

$$\overline{\tilde{\mathbf{u}}} = \frac{\overline{\rho \mathbf{u}}}{\rho_o} = \frac{\overline{\rho}}{\rho_o} \overline{\mathbf{u}}^{\rho}. \tag{9}$$

$\overline{\tilde{\mathbf{u}}}$ is the average mass flux per unit area normalised by a constant reference density ρ_o. Writing (5)-(7) in terms of $\tilde{\mathbf{u}}$ yields

$$(\overline{\rho}/\rho_o)_t + \nabla \cdot \overline{\tilde{\mathbf{u}}} = 0, \tag{10}$$

$$(\frac{\overline{\rho}}{\rho_o} \overline{C}^{\rho})_t + \nabla \cdot (\overline{\tilde{\mathbf{u}}}\ \overline{C}^{\rho}) = -\nabla \cdot (\overline{\rho \mathbf{u}'_{\rho} C'_{\rho}}) \tag{11}$$

$$\overline{\tilde{\mathbf{u}}}_t + \nabla \cdot (\frac{\rho_o}{\overline{\rho}} \overline{\tilde{\mathbf{u}}\tilde{\mathbf{u}}}) + 2\mathbf{\Omega} \times \overline{\tilde{\mathbf{u}}} = -\frac{1}{\rho_o} \nabla \overline{p} - \mathbf{k} g \frac{\overline{\rho}}{\rho_o} - \frac{1}{\rho_o} \nabla \cdot (\overline{\rho \mathbf{u}'_{\rho} \mathbf{u}'_{\rho}}). \tag{12}$$

For simplicity, the molecular diffusion and viscosity terms have been dropped in comparison with the turbulent diffusion terms. It should be noted that the instantaneous equations (1)-(3) can also be written in the form (10)-(12), with averaged quantities replaced by unaveraged quantities (in which case $\overline{C}^{\rho}$ becomes C) and the turbulent correlation terms replaced by their molecular equivalents.

The main advantage of writing the equations in the form (10)-(12) is their strong similarity to the equations carried by Boussinesq ocean models. This can be seen by comparing the two sets of equations, non-Boussinesq and Boussinesq, summarized in the Appendix (equations (34)-(36) and (40)-(42), respectively). Note that we have deliberately written the Boussinesq set (40)-(42) using $\overline{\tilde{\mathbf{u}}}$ as the velocity variable and $\overline{C}^{\rho}$ as the tracer variable. (As discussed in MGL, we believe this be the appropriate interpretation of the variables in Boussinesq ocean models.) It is the strong similarity between the two sets of equations that can be exploited to make an existing Boussinesq code fully non-Boussinesq. Indeed, there are only four locations where the factor $\overline{\rho}/\rho_o$ (or its reciprocal) needs to be added to the Boussinesq equations (40)-(42) to turn

them into the non-Boussinesq set (34)-(36). In Section 3. we discuss the detailed code modifications that are required to do this in the case of hydrostatic codes, and in Section 4 we note that the effect of these modifications in the case of the POP model is a modest $\approx 20\%$ increase in cpu requirement. It should be noted that (10)-(12) can also be used to formulate a fully non-hydrostatic, non-Boussinesq code, and also, in view of the remark following equation (12), to integrate the instantaneous equations of motion. Indeed, it should be noted that the same model code can be used to integrate the non-Boussinesq equations at any resolution, be it coarse resolution or eddy-resolving resolution. The averaging operator should be understood to mean 'averaging over unresolved processes', as when integrating current Boussinesq codes at different resolutions.

The kinematic boundary condition at the free surface

Before discussing the code modifications required to integrate (10)-(12), we must deal with the formulation of the kinematic boundary conditions at the ocean surface and the ocean floor. It is convenient, at the same time, to discuss the treatment of the freshwater flux boundary condition at the surface, extending the treatment of Huang(1993).

We must first define what we mean by the displacement, $\overline{\eta}$, of the free surface from mean sea level. This is not the same as the average of the instantaneous free surface displacement η. Rather $\overline{\eta}$ is defined, following Lu(2001), by making use of the mass budget for a column of fluid. In particular, it is clearly necessary that $\overline{\eta}$ satisfy

$$\frac{\partial}{\partial t}\int_{-h}^{\overline{\eta}} \frac{\overline{\rho}}{\rho_o} dz + \nabla_H \cdot \int_{-h}^{\overline{\eta}} \overline{\tilde{\mathbf{v}}} dz = -\frac{\rho_w}{\rho_o}\overline{(E-P-R)} \tag{13}$$

where here E, P and R denote evaporation, precipitation and river run-off, respectively, and ρ_w is the density of freshwater. The vertical coordinate z is referenced to mean sea level in (13), the ocean bottom is at $z = -h$, ∇_H is the horizontal gradient operator, and $\overline{\tilde{\mathbf{v}}}$ refers to the horizontal component of $\overline{\tilde{\mathbf{u}}}$. Equation(13) corresponds to equation(12) in

Lu(2001). Applying density-weighted averaging to the kinematic boundary condition at the bottom gives

$$\overline{\tilde{w}} = -\overline{\tilde{\mathbf{v}}} \cdot \nabla_H h \qquad at \quad z = -h. \tag{14}$$

Combining (13) and (14) with the vertical average of the continuity equation, (10), then gives

$$\overline{\tilde{w}} = (\overline{\rho}/\rho_o)\overline{\eta}_t + \overline{\tilde{\mathbf{v}}} \cdot \nabla_H \overline{\eta} + \frac{\rho_w}{\rho_o}\overline{(E - P - R)} \qquad at \quad z = \overline{\eta}. \tag{15}$$

Equation (15) corresponds to the usual kinematic boundary condition at the surface.

It should be noted that the freshwater flux $\overline{(E - P - R)}$ enters very naturally into the formulation for the surface boundary condition. Equation (15) is, therefore, an extension of the form of surface boundary condition proposed by Huang(1993). As Huang points out, ocean modellers often approximate the surface freshwater flux boundary condition as a boundary condition on salinity, not on the vertical velocity at the surface. (In Section 4, experiments are described using both forms of boundary condition.) If the freshwater flux boundary condition is applied to $\overline{\tilde{w}}$, as in (15), then it is important to ensure that a condition of zero flux of salt is applied at the surface in the salinity equation. Care is also required in the potential temperature and the momentum equations. In particular, consideration must be given to the potential temperature and the momentum of the precipitation and the river run-off. In what follows, it is assumed, for simplicity, that the potential temperature and the momentum of the precipitation and the river run-off is the same as that in the surface grid box of the ocean model.

3. Modification of a Boussinesq ocean model to make it non-Boussinesq

In this section we describe the code modifications to existing, hydrostatic Boussinesq models required so that these models integrate the hydrostatic version of the non-Boussinesq equations (10)-(12), plus the appropriate boundary conditions. For

convenience, we shall focus attention on the POP model, although the approach is actually quite general and can be easily applied to other codes.

The continuity equation

The most important difference between current Boussinesq code and our non-Boussinesq formulation is in the continuity equation

$$(\overline{\rho}/\rho_o)_t + \nabla \cdot \overline{\tilde{\mathbf{u}}} = 0, \tag{16}$$

We note immediately that one big advantage of our approach is that it is only a local time derivative of $\overline{\rho}$ that appears in (16), not a total derivative as is often thought to be the case. This is the most important reason our method requires only modest code changes. The appearance of a local time derivative, rather than a total derivative, also makes it easy to preserve the conservation properties of currently existing codes.

In most Boussinesq models, the Boussinesq form of (16), namely

$$\nabla \cdot \overline{\tilde{\mathbf{u}}} = 0, \tag{17}$$

is used to diagnose the vertical velocity by vertically integrating the horizontal divergence, $\delta = (\overline{\tilde{u}}_x + \overline{\tilde{v}}_y)$ (where, for convenience, plane Cartesian coordinates have been employed). Most models use the leap-frog scheme to do time stepping (apart from an occasional forward time step to prevent time splitting). Denoting the current time level by n, the next time level by $n+1$, and the old time level by $n-1$, the diagnosis of the vertical velocity takes place at time level n (in the POP code this is done as part of the process of advancing the tracer and the (baroclinic) velocities from time level $n-1$ to time level $n+1$). Since we wish to preserve the Boussinesq code as much as possible, it makes sense to continue to diagnose the vertical velocity in the same way as in the Boussinesq code.

To achieve this objective, we define a new density variable, ρ^*, by

$$\rho^{*n+1} = 2\overline{\rho}^n - \overline{\rho}^{n-1} \tag{18}$$

Noting that ρ^{*n+1} can also be written as

$$\rho^{*n+1} = \overline{\rho}^n + (\overline{\rho}^n - \overline{\rho}^{n-1}) \tag{19}$$

it can be seen that ρ^{*n+1} is a linear extrapolation of $\overline{\rho}$ from time level n to time level $n+1$, based on the change in $\overline{\rho}$ from time levels $n-1$ to n. Using ρ^*, we now finite difference the continuity equation as

$$\frac{1}{\rho_o}\{\frac{\rho^{*n+1} - \rho^{*n-1}}{2\Delta t}\} + \nabla \cdot \overline{\tilde{\mathbf{u}}}^n = 0 \tag{20}$$

where Δt is the time step between time levels $n-1$ and n. The spatial differencing of $\nabla \cdot \overline{\tilde{\mathbf{u}}}^n$ is the same as in currently existing Boussinesq code, and does not require change. Since ρ^{*n+1} and ρ^{*n-1} are both known at time level n (since they are defined using values of $\overline{\rho}$ at time level n or earlier), $\overline{\tilde{w}}$ can be determined diagnostically, as in currently existing code. Note that when integrating $\partial\overline{\tilde{w}}/\partial z$ to obtain $\overline{\tilde{w}}$, either of the numerical equivalent of boundary conditions (14) or (15) can be used (the POP model uses the surface boundary condition (15)). The non-Boussinesq form of these boundary conditions are a simple modification of the Boussinesq form currently used in models.

The tracer equation

Let us now consider the finite differencing of the tracer equation, (11), i.e.

$$(\frac{\overline{\rho}}{\rho_o}\overline{C}^{\rho})_t + \nabla \cdot (\overline{\tilde{\mathbf{u}}}\ \overline{C}^{\rho}) = \nabla \cdot (\mathbf{A_C} \nabla \overline{C}^{\rho}). \tag{21}$$

For convenience, the turbulent correlation term has been parameterized using a Fickian diffusion tensor $\mathbf{A_C}$ (note that $\mathbf{A_C}$ can have both a symmetric and an antisymmetric part, the latter accounting for the so-called "bolus flux" of tracer; Gent et al., 1995).

We begin by noting that if (a) $\mathbf{A_C} = 0$, (b) there is no flux of tracer through the boundaries (in particular, no surface flux), and (c) $\overline{(E - P - R)} = 0$ in (15), then (21) has the following properties:

(i) if $\overline{C}^{\rho} = 1$, (21) reduces to the continuity equation (16),

(ii) $\frac{d}{dt}\int_V \overline{\rho}\overline{C}^{\rho} dV = 0$ and

(iii) $\frac{d}{dt}\int_V \overline{\rho}(\overline{C}^{\rho})^2 dV = 0$

where V is the volume of the ocean. The Boussinesq equivalents of (ii) and (iii) are

(iv) $\frac{d}{dt}\int_V \overline{C}^{\rho} dV = 0$ and

(v) $\frac{d}{dt}\int_V (\overline{C}^{\rho})^2 dV = 0$

where $\overline{C}^{\rho}$ is the tracer variable carried by the Boussinesq model (see equation (41) in the Appendix). It is obviously desirable that the finite difference approximation to (21) has the properties (i)-(iii). Indeed, it is usual for Boussinesq ocean model codes to satisfy the Boussinesq equivalent (i.e. (i), (iv) and (v)). Note, in particular, that if property (i) is satisfied by the finite difference scheme, then if the tracer concentration, $\overline{C}^{\rho}$, is spatially uniform, and there is no forcing of the tracer equation to change $\overline{C}^{\rho}$, then $\overline{C}^{\rho}$ will remain unchanged for all time, as should be the case. We note that in Boussinesq models, (v) is a property of the spatial discretization only (there is usually an error in satisfying (v) associated with time stepping). Further, by finite differencing $\nabla \cdot (\overline{\tilde{\mathbf{u}}}\ \overline{C}^{\rho})$ in the same way as in the currently existing Boussinesq code, the proof of (iii) follows as for the proof of (v) for the Boussinesq code (see Semtner(1986), and note that the proof of (iii) makes use of the finite-difference continuity equation (20)).

To ensure that (i) and (ii) are satisfied, we finite difference the advection operator as follows:

$$(\frac{\overline{\rho}}{\rho_o}\overline{C}^{\rho})_t + \nabla \cdot (\overline{\tilde{\mathbf{u}}}\ \overline{C}^{\rho}) \approx \frac{1}{\rho_o}\{\frac{\rho^{*n+1}\overline{C}^{\rho\ n+1} - \rho^{*n-1}\overline{C}^{\rho\ n-1}}{2\Delta t}\} + \nabla \cdot (\overline{\tilde{\mathbf{u}}}\ \overline{C}^{\rho})^n \qquad (22)$$

where ρ^* is defined as in (18). Putting $\overline{C}^{\rho} = 1$, the finite difference tracer equation with $\mathbf{A_C} = 0$ now reduces to the finite difference continuity equation. It is now a simple matter, following the method in Semtner(1986), to show that property (ii) is satisfied by the finite differencing (note that in finite difference form, $\overline{\rho}$ in (ii) and (iii) is replaced by ρ^*). Also, since ρ^{*n+1} involves only known values of $\overline{\rho}$, updating $\overline{C}^{\rho}$ using (22) is

straightforward.

Next, we comment on the treatment of the turbulent mixing term $\nabla \cdot (\mathbf{A_C} \nabla \overline{C}^{\rho})$. Since the lateral mixing (horizontal or isopycnal) is usually treated explicitly, these terms require no change from their treatment in Boussinesq models. On the other hand, the vertical mixing term, which is usually treated implicitly, requires some care. To maintain the implicit treatment, it is convenient to write the finite difference operator in (22) in the equivalent form

$$\frac{1}{\rho_o}\{\rho^{*n+1}\frac{(\overline{C}^{\rho\ n+1} - \overline{C}^{\rho\ n-1})}{2\Delta t} + \overline{C}^{\rho\ n-1}\frac{(\rho^{*n+1} - \rho^{*n-1})}{2\Delta t}\} + \nabla \cdot (\tilde{\overline{\mathbf{u}}}\ \overline{C}^{\rho})^n \tag{23}$$

so that the term that updates $\overline{C}^{\rho}$, i.e. $\frac{\rho^{*n+1}(\overline{C}^{\rho\ n+1} - \overline{C}^{\rho\ n-1})}{2\Delta t}$, involves only the density ρ^{*n+1}. It is then a simple matter to modify the existing implicit treatment found in Boussinesq codes. In fact the matrix used for the implicit treatment is then the same as in the Boussinesq code, but with $2\Delta t$ replaced by $2\Delta t \rho_o / \rho^{*n+1}$, and with the addition of the forcing term $-\overline{C}^{\rho\ n-1}\frac{(\rho^{*n+1} - \rho^{*n-1})}{2\Delta t}$.

The momentum equation

We now turn to the momentum equation (12). We begin by noting that the expression for the kinetic energy of the mean flow can be deduced from (7) and is given by

$$KE = \frac{1}{2}\overline{\rho}\ \overline{\mathbf{u}}^{\rho} \cdot \overline{\mathbf{u}}^{\rho} \tag{24}$$

In the hydrostatic system we are considering, the contribution to the kinetic energy from the vertical velocity is neglected so that

$$KE = \frac{1}{2}\overline{\rho}\ \overline{\mathbf{v}}^{\rho} \cdot \overline{\mathbf{v}}^{\rho} \tag{25}$$

where $\overline{\mathbf{v}}^{\rho}$ is the horizontal component of $\overline{\mathbf{u}}^{\rho}$. Writing the horizontal component of (12) in the form

$$(\frac{\overline{\rho}}{\rho_o}\ \overline{\mathbf{v}}^{\rho})_t + \nabla \cdot (\tilde{\overline{\mathbf{u}}}\overline{\mathbf{v}}^{\rho}) + 2\mathbf{\Omega} \times \tilde{\overline{\mathbf{v}}} = -\frac{1}{\rho_o}\nabla_H \overline{p} + \nabla \cdot (\mathbf{A}\nabla \overline{\mathbf{v}}^{\rho}), \tag{26}$$

it is then easy to see that the energy equation is obtained by taking the dot product of $\overline{\mathbf{v}}^{\rho}$ with the horizontal momentum equation, as one would expect. As in the tracer equation, we have parameterized the turbulent mixing term on the right hand side using a Fickian diffusion tensor $\mathbf{A}$ that may have both an antisymmetric and a symmetric part. Note also that to ensure that energy is dissipated in the domain interior, it is very important that the velocity variable that appears in the mixing term is the density-weighted velocity, $\overline{\mathbf{v}}^{\rho}$, not $\overline{\tilde{\mathbf{v}}}$ ($\tilde{\mathbf{v}}$ is the horizontal component of $\tilde{\mathbf{u}}$). It should also be noted that the Coriolis and pressure gradient terms in (26) have the same form as in their Boussinesq counterpart (compare equations (36) and (42) in the Appendix). It follows that using the same finite differencing for these terms as in the Boussinesq model, the energy conservation properties of the code associated with these terms is the same as in Boussinesq codes, apart from the contribution that arises from the divergence of the density-weighted mean velocity, $\overline{\mathbf{u}}^{\rho}$ (this contribution represents an exchange of energy with the internal energy missing in Boussinesq models).

It remains, therefore, to examine the properties of the finite-difference advection operator, and the numerical treatment of the turbulent mixing terms. Since the local time derivative and the non-linear advection terms in (26) have the same form as in the tracer equation, (21), (with $\overline{C}^{\rho}$ replaced by $\overline{\mathbf{v}}^{\rho}$) it follows that the advection operator will conserve the kinetic energy (in the same sense as property (iii) is satisfied for the tracer equation) provided that the finite differencing of the advection operator in the momentum equation is equivalent to that in the tracer equation. In the case of POP, this condition is already satisfied by the Boussinesq code (Dukowicz et al., 1993). The non-Boussinesq code is complicated by the presence of two velocity variables, $\overline{\mathbf{v}}^{\rho}$ and $\overline{\tilde{\mathbf{v}}}$. In practice, it is convenient to carry $\overline{\tilde{\mathbf{v}}}$ as the velocity variable in the model, so it is very important that the conversion between $\overline{\tilde{\mathbf{v}}}$ and $\overline{\mathbf{v}}^{\rho}$ should be done correctly. This is guarenteed if

$$\overline{\tilde{\mathbf{v}}}_{i,j} = \overline{\rho^*}^{xy} \overline{\mathbf{v}}^{\rho}_{i,j} / \rho_o \tag{27}$$

where $\overline{\rho^*}^{xy}$ is the four point average of values of ρ^* centred around the i,jth $\mathbf{v}$ grid point (recall that POP uses an Arakawa B-grid for which both components of the horizontal velocity reside at the centre of a grid cell, with density stored at the corners of the grid cell). Finally, we note that since the lateral mixing of momentum is treated explicitly (as for the tracer equation), it is easy to modify existing code to take care of these terms, and the implicit treatment of vertical mixing can be treated in a manner similar to the tracer equation.

The free surface equation

The non-Boussinesq form of the free surface equation is obtained from (13) and is

$$(\overline{\rho}/\rho_o)\overline{\eta}_t = -\int_{-h}^{\overline{\eta}} \frac{\partial}{\partial t}[\frac{\overline{\rho}}{\rho_o}]dz - \nabla_H \cdot \int_{-h}^{\overline{\eta}} \overline{\tilde{\mathbf{v}}} dz - \frac{\rho_w}{\rho_o}\overline{(E-P-R)} \tag{28}$$

Its Boussinesq counterpart (excluding the freshwater flux) is

$$\overline{\eta}_t = -\nabla_H \cdot \int_{-h}^{\overline{\eta}} \overline{\tilde{\mathbf{v}}} dz \tag{29}$$

POP uses (29) to solve for the barotropic component of the flow using an implicit treatment described by Dukowicz and Smith(1994). (Note that the contribution of the (unknown) free surface displacement to the horizontal pressure gradient appears, through the $\nabla_H \cdot \int_{-h}^{\overline{\eta}} \overline{\tilde{\mathbf{v}}} dz$ term, as an elliptic operator acting on $\overline{\eta}$.) It is a simple matter to modify the finite differencing of (29) to integrate (28), ensuring consistency with the finite difference continuity equation (20), and the finite difference treatment of the kinematic boundary condition (15) used in the diagnosis of $\overline{\tilde{w}}$. In particular, the same treatment for the $\frac{\partial}{\partial t}(\overline{\rho}/\rho_o)$ term should be used as in the continuity equation.

The equation of state

It is common in ocean models to use the approximate equation of state

$$\rho \equiv \rho(\theta, S, p_{ref}) \tag{30}$$

where p_{ref} is a reference pressure that depends only on depth, and θ and S are the potential temperature and salinity variables carried by the model (and so are implicitly averaged, not instantaneous, quantities). In this way, most of the dependence of density on pressure is taken into account, but there is an error because the effect of pressure variations on density is not included. As discussed by Dewar et al.(1998), the effect of using (30) on the horizontal pressure gradients is to introduce an error of order $gh/{c_s}^2 \approx$ a few %, where g is the acceleration due to gravity, h is the depth of the ocean and c_s is the speed of sound. Since this error is the same order of magnitude as that associated with the Boussinesq approximation, we follow Dewar et al. and include the effect of pressure variations in the equation of state used to compute density in the hydrostatic equation; that is, we use (38) in the Appendix to compute density in the hydrostatic equation (37). (The use of averaged quantities to evaluate the equation of state is discussed in detail in MGL.) However, we use (39) rather than (38) to compute $(\overline{\rho}/\rho_o)_t$ in the continuity equation (or in the free surface equation), because to use (38) would introduce sound waves into our model formulation, and would place a severe limit on the allowable time step and the model performance. The error introduced by doing this is only a few tenths of 1 %, and so is small even to the order of accuracy of our non-Boussinesq code.

4. Comparing Non-Boussinesq and Boussinesq model runs

We are now ready to compare the behaviour of our non-Boussinesq code with its Boussinesq counterpart. The equations governing both the non-Boussinesq and Boussinesq models are summarized in the Appendix.

An eddy-permitting calculation

We begin by comparing Boussinesq and non-Boussinesq model simulations of a closed, flat-bottomed basin under double gyre wind forcing. The computations use

spherical geometry, with the centre of the basin at 45^oN and a resolution of $1/5^o$ in both latitude and longitude. The basin extends across 20^o of latitude and 10^o of longitude, making 100 grid points in the north/south direction and 50 grid points in the east/west direction. There are 10 levels in the vertical, each of 100m thickness, making a total depth of 1000m. The wind stress has a cosine profile with maximum magnitude of 0.2N m^{-2} and is turned on suddenly at the start of the integration. The vertical eddy viscosity and diffusivity are 10^{-3} and $10^{-4}m^2s^{-1}$, respectively, and Laplacian mixing is used in the horizontal with a coefficient of $100m^2s^{-1}$ for both momentum and tracers. Both the Boussinesq and non-Boussinesq models are initialised with a state of rest, uniform salinity and with potential temperature, θ, a function of depth only given by $\theta = \theta(z)$. There is no freshwater flux forcing (so salinity remains uniform and constant), but the interior temperature is restored back to the initial temperature profile on a time scale of 1 year.

Following an initial adjustment, both models reach a statistically steady state. Figure 1 shows the mean sea surface height (SSH) from the two models, and their difference, averaged from year 20 to year 50. It should be noted that extending the averaging period from year 10 to year 50 makes no significant difference to the figures, indicating that both models are in a statistically steady state and that the averaging period is long enough that the difference between the model solutions is stable and consistent. It is clear that, apart from an offset in the mean SSH to be discussed in the next paragraph, the two SSH fields look very similar. The difference field indicates that the use of the Boussinesq model is associated with an error of less than 5% in the mean fields, as is normally associated with the Boussinesq approximation. We also computed EOF's (Empirical Orthogonal Functions) using weekly averages of SSH (with the spatial mean removed in the non-Boussinesq case, see below) from the first 50 years of the integrations. For both model runs, the first two EOF's account for roughly 35% each of the SSH variance, and have very similar spatial structure in both the

Boussinesq and non-Boussinesq model runs. In both cases, these EOF's are associated with a quasi-periodic penetration of the separated jet into the domain interior and its subsequent break down. Figure 2 compares the time series of the first EOF from both models. It is clear that for the first several years or so, the principal component time series from both models are similar, after which they have a tendency to become increasingly separated from each other. It follows that it is only on these long time scales that there is any significant difference between the model solutions. (It should noted that the time required for the two model solutions to become separated depends on the model problem one is considering. In companion experiments in which the strength of the wind forcing is doubled, the two models become separated within the second year. We attribute the more rapid separation to the more highly turbulent model behaviour in this case.)

We have also run the non-Boussinesq model excluding the effect of pressure variations from the equation of state; that is, using (39) in the hydrostatic equation, rather than (38). The results show a difference in model behaviour that is similar in character to the difference between the Boussinesq and non-Boussinesq models shown in Figures 1 and 2. This is consistent with our conclusion that the error in using (39) in the hydrostatic relation, pointed out by Dewar et al.(1998), is similar in magnitude to the error associated with using the Boussinesq approximation.

An, at first, unexpected feature of the model solutions is the offset in the mean SSH in the non-Boussinesq model. Figure 3 shows the time evolution of the basin mean SSH (which remains zero in the Boussinesq model) from the standard run, in which the temperature field carried by the model is restored back to the initial temperature on a time scale of 1 year, and a case in which there is no interior restoring. In both cases, the basin mean SSH reduces with time, the drop in mean sea level being the greatest in the run with no interior restoring. An companion run of the non-Boussinesq model using a linear equation of state shows no drop in mean SSH, indicating that the drop

in mean SSH is a consequence of the non-linear equation of state; in fact, the so-called "densification on mixing" (McDougall and Garrett, 1992). In particular, the vertical and horizontal diffusion of heat leads to a net increase in density, and hence a drop in mean SSH to conserve mass. It is interesting to note that in the absense of surface buoyancy forcing, mean sea level in the ocean would drop because of the non-linear equation of state. Mixing up the entire initial temperature profile in our basin leads to a drop in mean sea level of about 16 cm.

A coarse-resolution global model with seasonal forcing

Next we compare Boussinesq and non-Boussinesq versions of a coarse resolution global ocean model with seasonal forcing. The model has the same resolution as the ocean component of the GFDL coupled model used by Delworth et al.(1993). In particular, the horizontal resolution is 4.5^o in latitude and 3.75^o in longitude and there are 12 unevenly spaced levels in the vertical. Both models are forced by seasonally varying monthly mean surface wind stress. To begin, a spin-up calculation was carried out using the Boussinesq model by restoring the temperature and salinity in the top vertical level of the model to seasonally varying monthly mean surface temperature and salinity taken from the Levitus(1982) climatology. The restoring times are 30 days for temperature and 50 days for salinity. Once a seasonally varying equilibrium was reached, the monthly mean surface heat and freshwater fluxes were diagnosed and these fluxes, together with the seasonally varying surface wind stress, were then used to drive both the Boussinesq and non-Boussinesq models initialised with the same state (January 1) from the Boussinesq spin-up. Two non-Boussinesq model runs were carried out. In the first, the freshwater flux was implemented as a "virtual" salt flux (that is as a flux boundary condition on the surface salinity; Huang, 1993). In the second run, an equivalent freshwater flux was diagnosed from the diagnosed salt flux and this was then implemented as a boundary condition on $\overline{\tilde{w}}$ at the surface as in equation (15) (the

so-called "real freshwater flux" boundary condition; Huang, 1993), together with the appropriate surface boundary conditions on the other model variables, as discussed at the end of Section 2.

Figure 4 shows time series of globally averaged SSH from the two non-Boussinesq runs and the companion Boussinesq run. Since the Boussinesq model conserves volume, the global mean SSH remains constant in time (at value zero). In the non-Boussinesq model this constraint is released. The model now conserves mass and not volume, and there is a seasonal variation in global mean SSH. The case that uses a "virtual" salt flux boundary condition on the surface salinity shows the seasonal variation of mean sea level due to the steric expansion effect. As can be seen, the seasonal range is about 0.7 cm. Both the amplitude and the phase are in general agreement with the estimate of this quantity given in Figure 11 of Mellor and Ezer(1995) based on the Levitus(1982) climatology. The maximum occurs as the end of the southern hemisphere summer, with a weak secondary peak at the end of the northern hemisphere summer. The dominance of the southern hemisphere is a consequence of the ocean occupying a much larger proportion of the southern hemisphere than is the case in the northern hemisphere. When the freshwater flux is applied as a boundary condition on $\overline{\tilde{w}}$, the freshwater flux can also change the mass of the ocean and hence influence the global mean SSH. Clearly, in our model, this effect is more important than the steric sea level effect, the seasonal range is global mean SSH being about 3 cm in this case.

Although global mean SSH remains unchanged in the Boussinesq model, we can diagnose its seasonal cycle from the Boussinesq model output, following Greatbatch(1994). The contribution from the steric expansion effect agrees very closely with the non-Boussinesq model. In the case of the freshwater flux forcing, the diagnosed seasonal cycle is set by the global average of the specified freshwater flux entering the ocean, and so is, a priori, in close agreement with the non-Boussinesq model.

Figure 5 shows a comparison between the three model runs and the seasonal

cycle of SSH as measured by the TOPEX-POSEIDON altimeter in two regions of the southern hemisphere (see the figure caption for the details). The Boussinesq model, and the "virtual" salt flux version of the non-Boussinesq model, both overestimate the seasonal cycle in SSH in these two regions. On the other hand, applying the freshwater water flux as a boundary condition on $\overline{\tilde{w}}$, and hence including the freshwater flux in the mass budget of the model, clearly improves the comparison between the model and the altimeter data. It should be noted that adding the seasonal cycle in global mean SSH shown in Figure 4 to the Boussinesq model result leads to a seasonal cycle that is almost indistinguishable, in both regions, from that in the non-Boussinesq model with the real freshwater flux boundary condition. It follows that on the seasonal time scale, the Boussinesq model can be adjusted by a globally uniform correction to reproduce the non-Boussinesq model result, as suggested by Greatbatch(1994). Use of the non-Boussinesq model to compute SSH nevertheless has the advantage that the SSH is computed prognostically, without the need to make time-varying diagnostic corrections.

We have also compared the spatial structure of SSH in the two models. An example is shown in Figure 6. The difference fields (non-Boussinesq minus Boussinesq) have a surprising amount of structure, with spatial variations of several centimeters not captured by a globally uniform correction. The spatial structure evolves slowly over the 10 years of the model runs and does not appear to project strongly on to the seasonal cycle. Compared to the spatial variation of the total field, where the range is of order a meter, the difference field is within the 5 % error bar expected from the Boussinesq approximation. Nevertheless, locally, the difference between the non-Boussinesq and Boussinesq model SSH can be significant. A feature of Figure 6 is the checkerboard pattern seen in the lower panel. The checkerboard pattern is a well known feature of the free surface finite-difference equation on the B-grid (Killworth et al., 1991; Dukowicz et al., 1993). We have found that applying the freshwater flux as a boundary condition

on $\overline{\tilde{w}}$ (as in (15)) tends to excite the checkboard noise. A method of controlling the checkerboarding has been suggested by Killworth et al.(1991).

To further estimate the importance of non-Boussinesq effects in our global model, we use a technique based on the method of Lu(2001). We begin by noting that the continuity equation is

$$(\overline{\rho}/\rho_o)_t + \nabla \cdot \overline{\tilde{\mathbf{u}}} = 0 \tag{31}$$

We now define a new velocity variable by

$$\hat{\mathbf{u}} = \overline{\tilde{\mathbf{u}}} + \delta w \hat{\mathbf{k}} \tag{32}$$

and choose δw so that $\nabla \cdot \hat{\mathbf{u}} = 0$ everywhere, and $\delta w = 0$ at the ocean bottom. It follows that

$$\delta w = \int_{-h}^{z} \frac{\partial}{\partial t}[\frac{\overline{\rho}}{\rho_o}]dz. \tag{33}$$

δw measures the contribution to $\overline{\tilde{w}}$ associated with the divergence of the $\overline{\tilde{\mathbf{u}}}$ velocity field. Figure 7 shows a plot of the log of the inverse of $rms(\overline{\delta w})/rms(\overline{\tilde{w}})$ at the base of the grid box at the surface of the model, where rms denotes the root mean square computed using model output every time step over a 10 year period. It is clear that over most of the model domain $rms(\overline{\delta w})/rms(\overline{\tilde{w}})$ is less than 1 %, but there are a few isolated locations where the ratio exceeds 10 %.

5. Summary and conclusions

In this paper, we have shown that existing, hydrostatic Boussinesq ocean model codes can easily be modified to integrate the hydrostatic, non-Boussinesq equations written in terms of $\overline{C}^{\rho}$ and $\overline{\tilde{\mathbf{u}}}$ (where here C is either potential temperature or salinity). $\overline{C}^{\rho}$ is the density-weighted average of C, and $\overline{\tilde{\mathbf{u}}}$ is the average mass flux per unit area divided by a constant reference density. We illustrated the method for the case of POP, the parallel version of the Bryan/Cox/Semtner code developed at Los Alamos National Laboratory. The associated increase in cpu requirement is modest ($\approx$ 20 %

for POP). A comparison of model solutions for the case of eddy permitting calculations under double gyre wind forcing shows that the error involved in making the Boussinesq approximation is reassuringly within a few percent. We also compared Boussinesq and non-Boussinesq versions of a coarse resolution global ocean model under seasonal forcing. The non-Boussinesq model shows a seasonal variation in global mean sea surface height (SSH) with a range of about 3 cm, mostly attributable to changes in the mass of the ocean due to the freshwater flux forcing, but with a ≈ 25 % contribution from the steric expansion effect. We also compared the seasonal cycle of model-computed SSH with TOPEX-POSEIDON data from both the South Pacific and South Atlantic Oceans. Taking proper account of the global mass budget improves the agreement between the model and the data. We also found that the seasonal cycle in the non-Boussinesq model can be reproduced by adding the seasonal cycle in global mean SSH to the seasonal cycle in the Boussinesq model, confirming the suggestion of Greatbatch(1994). A non-Boussinesq model nevertheless has the advantage that SSH is computed prognostically, without the need to make diagnostic corrections, and is consequently a more convenient vehicle for assimilating SSH or bottom pressure data than a Boussinesq model. On longer time scales, we noted that the difference in SSH between the Boussinesq and non-Boussinesq models shows a surprising amount of structure, with spatial variations of several centimeters that cannot be accounted for by a globally uniform offset.

Acknowledgments. RJG is grateful for funding support from the Canadian Institute for Climate Studies, NSERC, the Meteorological Service of Canada and MARTEC, a Halifax company. Youyu Lu is supported by the Canada NCE program through the GEOIDE project, and Yi Cai is grateful to the Chinese Government for funding support that enabled her to visit Dalhousie University. Discussions with Trevor McDougall over the years have greatly influenced our thinking on this problem. We also wish to thank Professor Jürgen Willebrand for helpful comments and for pointing out the importance of including the effect of pressure

variations on density, as discussed by Dewar et al.(1998). We are also grateful to John Dukowicz, Stephen Griffies and Xin Huang for comments that have helped improve this work.

Appendix

We summarise our model equations, appropriate to both Boussinesq and non-Boussinesq model codes. The tracer variable is $\overline{C}^{\rho}$, the density-weighted mean, and the velocity variable is $\tilde{\overline{\mathbf{u}}}$, the average mass flux divided by a reference density, ρ_o (see equation (9)). $\tilde{\overline{\mathbf{v}}}$ is the horizontal component of $\tilde{\overline{\mathbf{u}}}$.

First, the equations governing our non-Boussinesq model are:

the continuity equation

$$(\overline{\rho}/\rho_o)_t + \nabla \cdot \tilde{\overline{\mathbf{u}}} = 0, \tag{34}$$

the tracer equation

$$(\frac{\overline{\rho}}{\rho_o}\overline{C}^{\rho})_t + \nabla \cdot (\tilde{\overline{\mathbf{u}}}\ \overline{C}^{\rho}) = \nabla \cdot (\mathbf{A_C} \nabla \overline{C}^{\rho}), \tag{35}$$

the horizontal momentum equation

$$(\tilde{\overline{\mathbf{v}}})_t + \nabla \cdot (\frac{\rho_o}{\overline{\rho}}\tilde{\overline{\mathbf{u}}}\ \tilde{\overline{\mathbf{v}}}) + 2\mathbf{\Omega} \times \tilde{\overline{\mathbf{v}}} = -\frac{1}{\rho_o}\nabla_H \overline{p} + \nabla \cdot (\mathbf{A} \nabla [\frac{\rho_o}{\overline{\rho}}\tilde{\overline{\mathbf{v}}}]). \tag{36}$$

the hydrostatic equation

$$\frac{\partial \overline{p}}{\partial z} = -g\overline{\rho} \tag{37}$$

the equation of state

$$\overline{\rho} = \rho(\overline{\theta}^{\rho}, \overline{S}^{\rho}, \overline{p}) \tag{38}$$

and, for use in (34),

$$\overline{\rho} = \rho(\overline{\theta}^{\rho}, \overline{S}^{\rho}, p_{ref}) \tag{39}$$

where p_{ref} is a depth dependent reference pressure, θ is potential temperature and S is salinity. The use of the two forms of the equation of state filters out sound waves. Note also that the use of averaged quantities in the evaluation of the equation of state to obtain the averaged density is discussed in detail in MGL. Finally, the kinematic boundary conditions at the free surface and the ocean bottom are given by (15) and (14), respectively.

The Boussinesq equivalent of (34)-(39) is

$$\nabla \cdot \tilde{\overline{\mathbf{u}}} = 0, \tag{40}$$

$$\overline{C}^{\rho}_t + \nabla \cdot (\tilde{\overline{\mathbf{u}}}\ \overline{C}^{\rho}) = \nabla \cdot (\mathbf{A_C} \nabla \overline{C}^{\rho}), \tag{41}$$

$$(\tilde{\overline{\mathbf{v}}})_t + \nabla \cdot (\widetilde{\overline{\mathbf{u}}\overline{\mathbf{v}}}) + 2\boldsymbol{\Omega} \times \tilde{\overline{\mathbf{v}}} = -\frac{1}{\rho_o}\nabla_H \overline{p} + \nabla \cdot (\mathbf{A}\nabla\tilde{\overline{\mathbf{v}}}). \tag{42}$$

$$\frac{\partial \overline{p}}{\partial z} = -g\overline{\rho} \tag{43}$$

and the equation of state

$$\overline{\rho} = \rho(\overline{\theta}, \overline{S}, p_{ref}) \tag{44}$$

Note that to within the accuracy of the Boussinesq system, we do not think it is necessary to include the effect of pressure variations on density in the hydrostatic relation (Dewar et al., 1998), although this effect is included in our non-Boussinesq system (equation (38)). As discussed in MGL, we recommend that the velocity variable in Boussinesq ocean models be interpreted as the averaged mass flux per unit area divided by a constant reference density (i.e. $\tilde{\overline{\mathbf{u}}}$), as written in (40)-(42).

References

Batchelor, G. K., 1967: An Introduction to Fluid Dynamics. Cambridge University Press, Cambridge, 615pp.

Delworth, T.L., S. Manabe and R.J. Stouffer, 1993: Interdecadal variations of the thermohaline circulation in a coupled ocean-atmosphere model. *J. Climate*, 6, 1993-2011.

Dewar, W. K., Y. Hsueh, T. J. McDougall and D. Yuan, 1998: Calculation of pressure in ocean simulations. *J. Phys. Oceanogr.*, **28**, 577-588.

Dukowicz, J. K., 1997: Steric sea level in the Los Alamos POP code - non-Boussinesq effects. In *Numerical Methods in Atmospheric and Oceanic Modeling, The Andre Robert Memorial Volume* (C. Lin, R. Laprise and H. Ritchie, Eds.), NRC Research Press, Ottawa, p533-546.

Dukowicz, J. K. and R. D. Smith, 1994: Implicit free-surface method for the Bryan-Cox-Semtner ocean model. *J. Geophys. Res.*, **99**, 7991-8014.

Dukowicz, J. K., R.D. Smith and R.C. Malone, 1993: A reformulation and implementation of the Bryan-Cox-Semtner ocean model on the connection machine. *J. Atmos. Ocean. Tech.*, 10, 195-208.

Favre A., 1965a: Équations des gaz turbulents compressibles I.- Forms générals. *Journal de Méchanique*, **4**, 361-390.

Favre A., 1965b: Équations des gaz turbulents compressibles II.- Méthode des vitesses moyennes; méthode des vitesses macroscopiques pondérées par la masse volumique. *Journal de Méchanique*, **4**, 391-421.

Gent, P.R., J. Willebrand, T.J. McDougall and J.C. McWilliams, 1995: Parameterizing eddy-induced transports in ocean circulation models. *J. Phys. Oceanogr.*, 25, 463-474.

Gill, A. E., 1982: *Atmosphere-Ocean Dynamics*, Academic Press. 662pp.

Greatbatch, R. J., 1994: A note on the representation of steric sea level in models that conserve volume rather than mass. *J. Geophys. Res.*, **99**, 12,767-12,771.

Huang, R.X., 1993: Freshwater flux as a natural boundary condition for the salinity balance and thermalhaline circulation forced by evaporation and precipitation. *J. Phys.*

Oceanogr., **23**, 2428-2446.

Huang, R.X., X. Jin and X. Zhang, 2001a: An oceanic general circulation model in pressure coordinates. *Advances in Atmospheric Science*, in press.

Huang, R.X. and X. Jin, 2001b: Sea surface elevation and bottom pressure anomalies due to thermohaline forcing, Part 1: isolated perturbations. *J. Phys. Oceanogr.*, submitted.

Hughes, C.W., C. Wunsch and V. Zlotnicki, 2000: Satellite peers through the oceans from space. *EOS*, 81(7), Feb 15 2000, 68.

Killworth, P.D., D. Stainforth, D.J. Webb and S.M. Paterson, 1991: The development of a free-surface Bryan-Cox-Semtner ocean model. *J. Phys. Oceanogr.*, 21, 1333-1348.

Levitus, S., 1982: Climatological Atlas of the World Ocean. *NOAA Prof. Pap. 13*, U.S. Dept. of Commerce, Washington D.C., 173pp.

Lu, Y., 2001: Including non-Boussinesq effects in Boussinesq ocean circulation models. *J. Phys. Oceanogr.*, in press.

McDougall, T. J. and C. J. R. Garrett, 1992: Scalar conservation equations in a turbulent ocean. *Deep-Sea Res.*, **39**, 1953-1966.

McDougall, T. J., R. J. Greatbatch and Y. Lu, 2001: On the conservation equations in oceanography: How accurate are Boussinesq ocean models? *J. Phys. Oceanogr.*, submitted.

Mellor, G. L. and T. Ezer, 1995: Sea level variations induced by heating and cooling: An evaluation of the Boussinesq approximation in ocean models. *J. Geophys. Res.*, **100**, 20,565-20,577.

Semtner, A.J., Jr., 1986: Finite-difference formulation of a world ocean model. In "Advanced Physical Oceanographic Modelling" , Ed. J.J. O'Brien, NATO ASI Series, Reidel Publishing Company, Dordrecht, 608pp.

This manuscript was prepared with the AGU LaTeX macros v3.1.

Figure Captions

Figure 1. Sea surface height (SSH) averaged from model years 20 to 50, for (a) the Boussinesq run and (b) the non-Boussinesq run of the eddy-permitting simulation. Panel (c) shows the difference, (a) minus (b). The contour interval is 5 cm in (a) and (b), and 0.5 cm in (c). Negative values are shown by dashed lines.

Figure 2. The principal component time series of the first EOF, computed from weekly averages of SSH from the eddy-permitting simulation. The thick line is for the non-Boussinesq run and the thin line for the Boussinesq run. Only the first 20 model years is shown.

Figure 3. Time evolution of the domain averaged SSH from the eddy-permitting simulation. The solid line depicts the solution of the non-Boussinesq run with interior restoring of temperature included. The dashed line depicts the non-Boussinesq run without temperature restoring. The dot-dashed line shows the solution of the Boussinesq run.

Figure 4. Time evolution of the domain averaged SSH from the coarse resolution global ocean simulation. The dashed line depicts the solution of the Boussinesq run; the thicker solid line depicts the non-Boussinesq run with the "virtual" salt flux surface boundary condition; and the thinner solid line depicts the non-Boussinesq run with the "real freshwater flux" surface boundary condition.

Figure 5. The seasonal cycle of SSH averaged over (a) the South Pacific and (b) the South Atlantic oceans. The heavy solid line depicts the TOPEX-POSEIDON data; the dot-dash line is from the Boussinesq model run; the thin solid line is from the non-Boussinesq run that uses the "virtual" salt flux surface boundary condition, and the dashed line is from the non-Boussinesq model with the "real freshwater flux" boundary condition. In (a), both the altimeter and model data have been averaged over the region bounded by $32^oS, 49^oS, 157^oE$ and 83^oE, and in (b) over the region bounded by $32^oS, 49^oS, 37^oW$ and 7^oE.

Figure 6. Differences of the monthly-mean SSH in April (model month) of year 10 between

different runs of the global simulation. (a) shows the non-Boussinesq run with salt flux boundary condition minus the Boussinesq run; (b) shows the non-Boussinesq run with freshwater flux boundary condition minus the non-Boussinesq run with salt flux boundary condition. The contour labels are in cm.

Figure 7. The spatial distribution of $\log_{10}\{rms(\overline{\tilde{w}})/rms(\delta w)\}$, where rms denotes root mean square (see text for details). Both $rms(\delta w)$ and $rms(\overline{\tilde{w}})$ are calculated at the base of the grid box at the surface of the model. The area with $\log_{10}\{rms(\overline{\tilde{w}})/rms(\delta w)\} > 2.5$ is unshaded, otherwise the shading is as shown to the right of the figure. The dashed contours depict $\log_{10}\{rms(\overline{\tilde{w}})/rms(\delta w)\} = 2$, and the solid contours depict $\log_{10}\{rms(\overline{\tilde{w}})/rms(\delta w)\} = 1$.

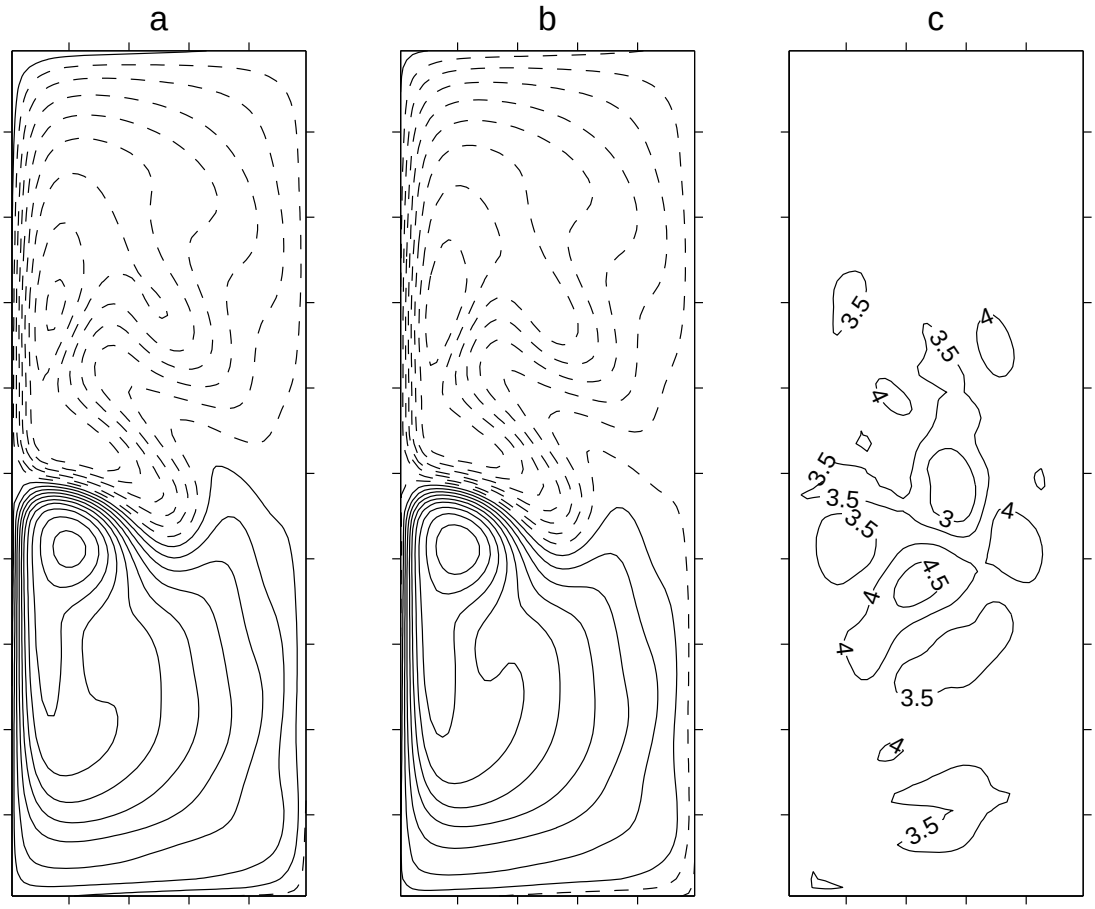

Figure 1. Sea surface height (SSH) averaged from model years 20 to 50, for (a) the Boussinesq run and (b) the non-Boussinesq run of the eddy-permitting simulation. Panel (c) shows the difference, (a) minus (b). The contour interval is 5 cm in (a) and (b), and 0.5 cm in (c). Negative values are shown by dashed lines.

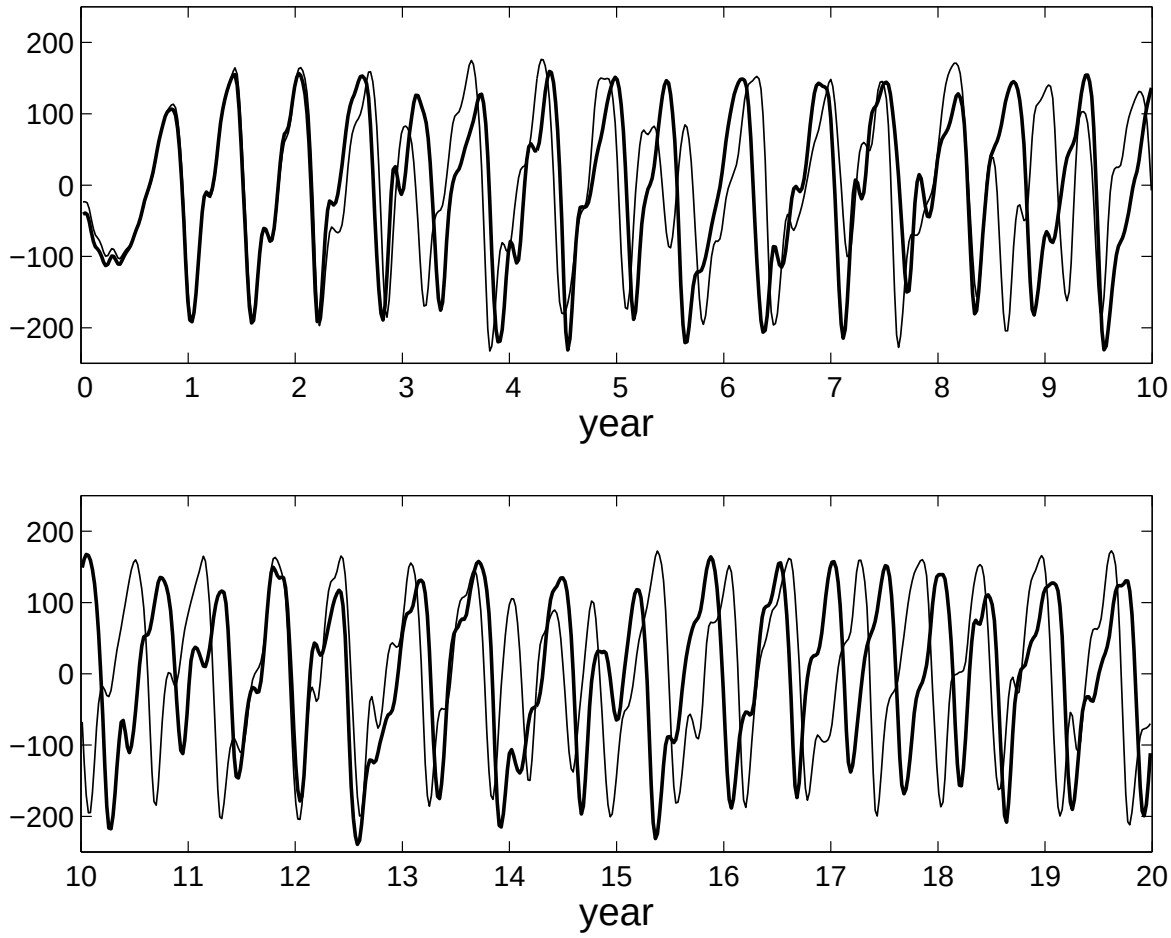

Figure 2. The principal component time series of the first EOF, computed from weekly averages of SSH from the eddy-permitting simulation. The thick line is for the non-Boussinesq run and the thin line for the Boussinesq run. Only the first 20 model years is shown.

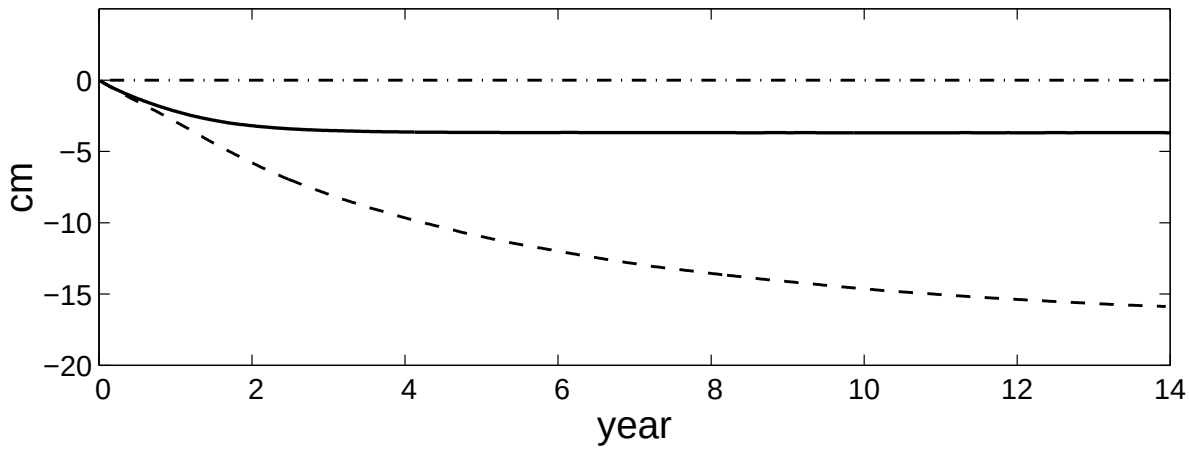

Figure 3. Time evolution of the domain averaged SSH from the eddy-permitting simulation. The solid line depicts the solution of the non-Boussinesq run with interior restoring of temperature included. The dashed line depicts the non-Boussinesq run without temperature restoring. The dot-dashed line shows the solution of the Boussinesq run.

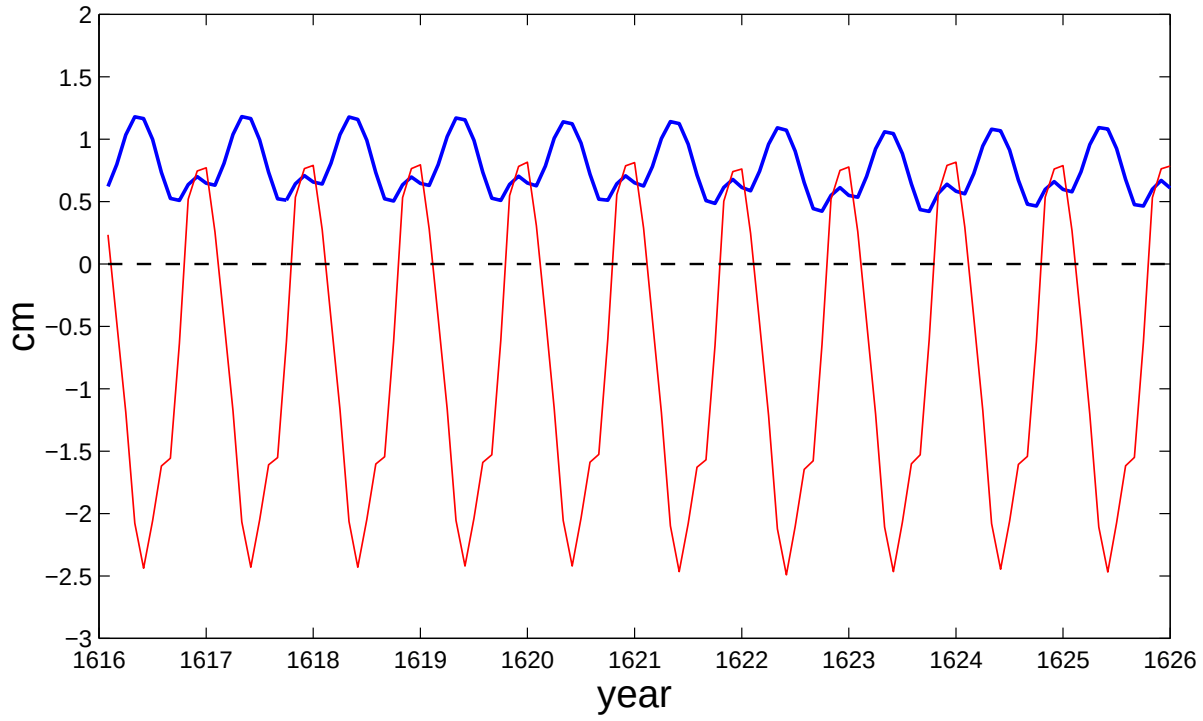

Figure 4. Time evolution of the domain averaged SSH from the coarse resolution global ocean simulation. The dashed line depicts the solution of the Boussinesq run; the thicker solid line depicts the non-Boussinesq run with the "virtual" salt flux surface boundary condition; and the thinner solid line depicts the non-Boussinesq run with the "real freshwater flux" surface boundary condition.

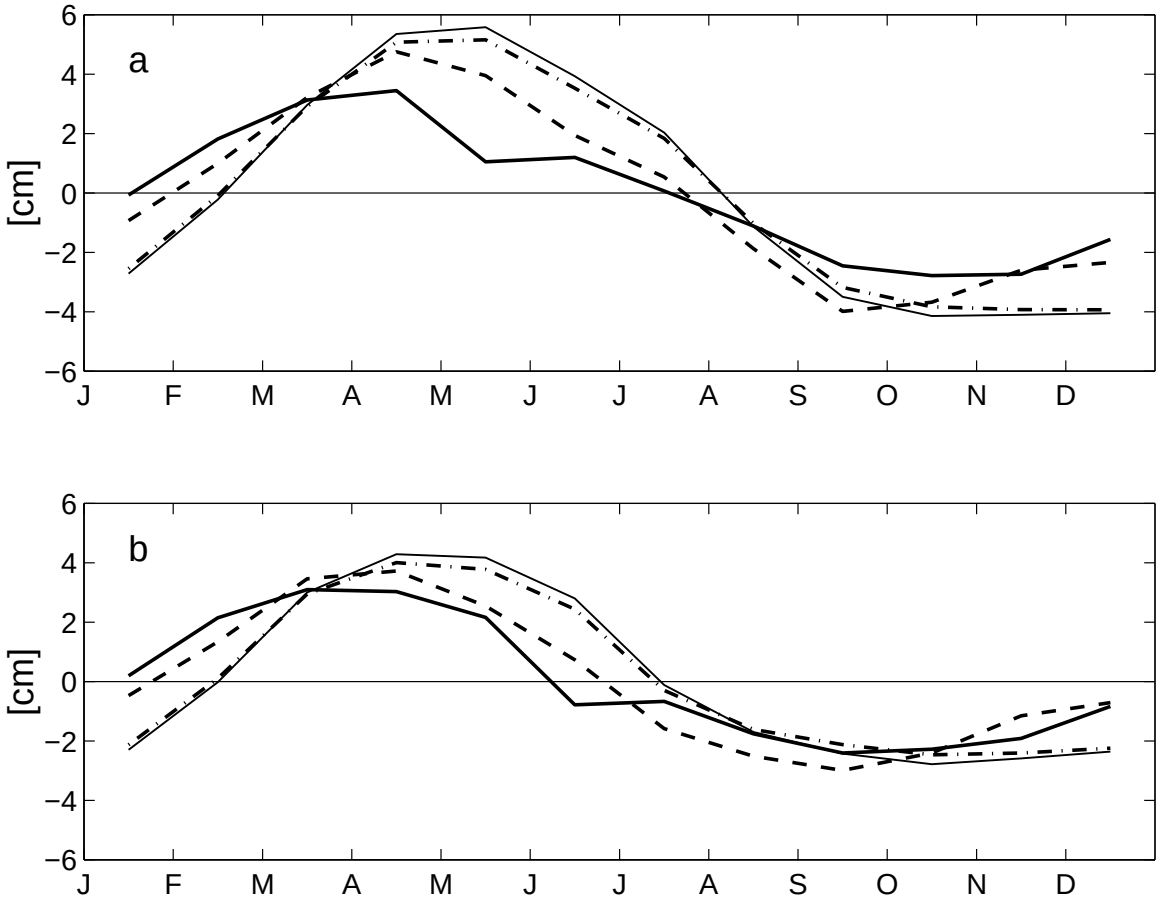

Figure 5: The seasonal cycle of SSH averaged over (a) the South Pacific and (b) the South Atlantic oceans. The heavy solid line depicts the TOPEX-POSEIDON data; the dot-dash line is from the Boussinesq model run; the thin solid line is from the non-Boussinesq run that uses the "virtual" salt flux surface boundary condition, and the dashed line is from the non-Boussinesq model with the "real freshwater flux" boundary condition. In (a), both the altimeter and model data have been averaged over the region bounded by $32^oS, 49^oS, 157^oE$ and 83^oE, and in (b) over the region bounded by $32^oS, 49^oS, 37^oW$ and 7^oE.

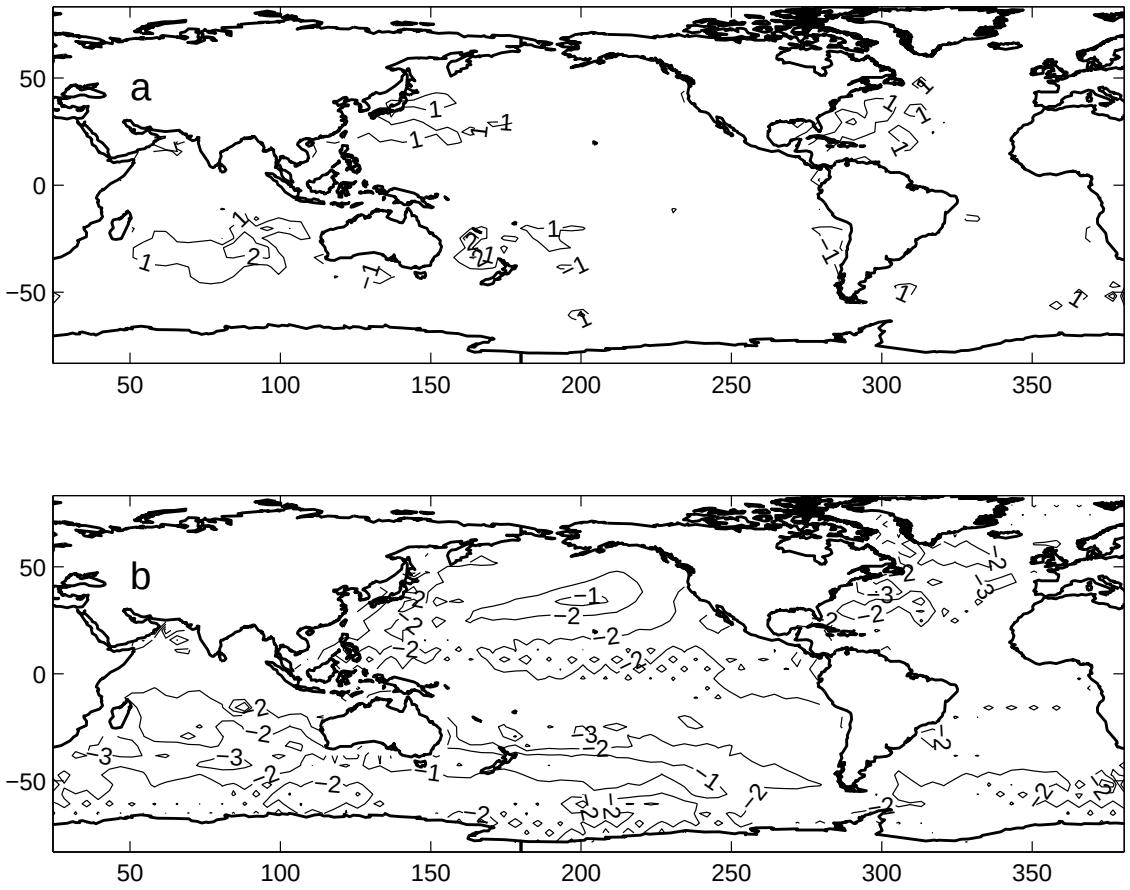

Figure 6. Differences of the monthly-mean SSH in April (model month) of year 10 between different runs of the global simulation. (a) shows the non-Boussinesq run with salt flux boundary condition minus the Boussinesq run; (b) shows the non-Boussinesq run with freshwater flux boundary condition minus the non-Boussinesq run with salt flux boundary condition. The contour labels are in cm.

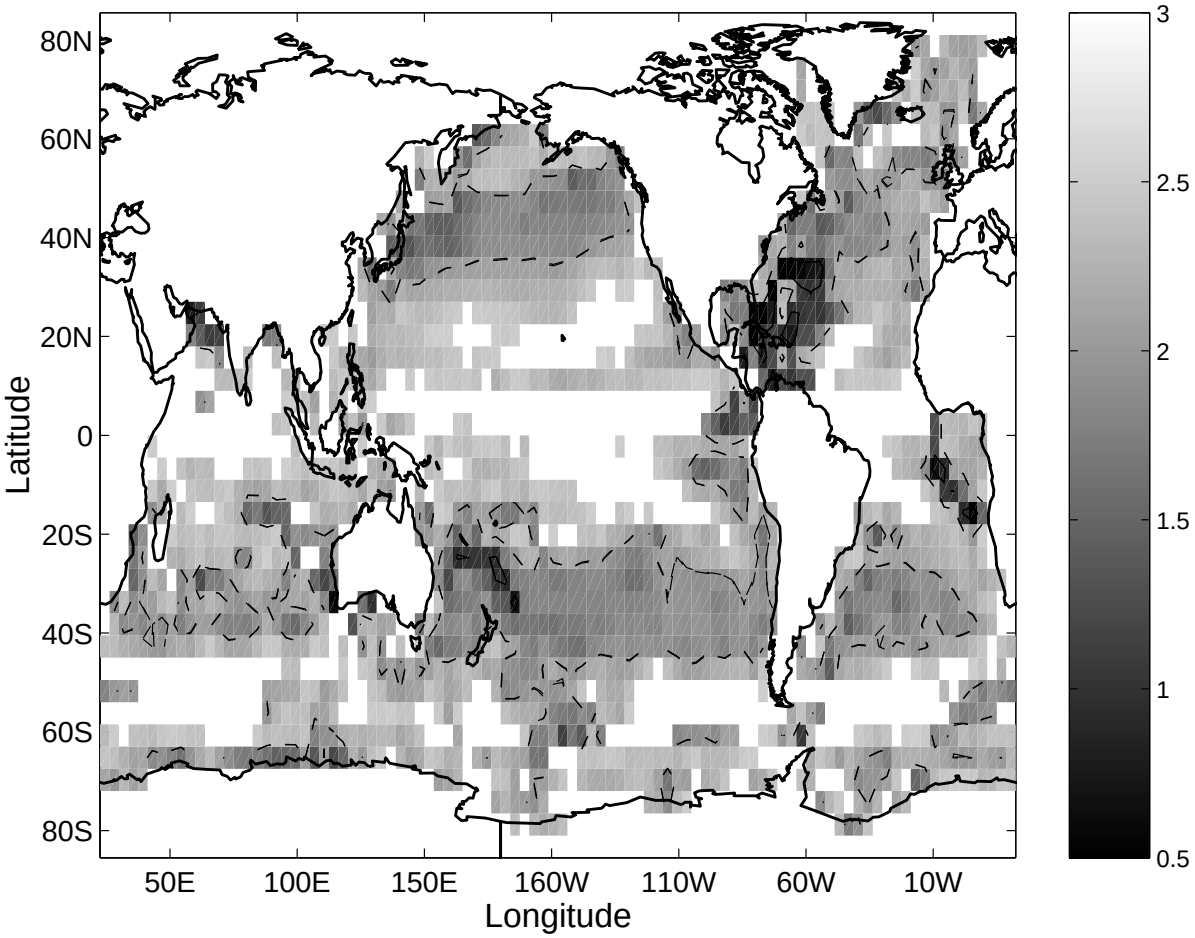

Figure 7. The spatial distribution of $\log_{10}\{rms(\overline{\tilde{w}})/rms(\delta w)\}$, where rms denotes root mean square (see text for details). Both $rms(\delta w)$ and $rms(\overline{\tilde{w}})$ are calculated at the base of the grid box at the surface of the model. The area with $\log_{10}\{rms(\overline{\tilde{w}})/rms(\delta w)\} > 2.5$ is unshaded, otherwise the shading is as shown to the right of the figure. The dashed contours depict $\log_{10}\{rms(\overline{\tilde{w}})/rms(\delta w)\} = 2$, and the solid contours depict $\log_{10}\{rms(\overline{\tilde{w}})/rms(\delta w)\} = 1$.